論文 / 著書情報
Article / Book Information

Title	Strength-limiting defects evolved from heterogeneities during the sintering of high-purity submicron alumina powder
Authors	Gaku Okuma, Tsukasa Shimizugawa, Shingo Ozaki, Toshio Osada, Shingo Machida, Yutaro Arai, Ryo Inoue, Hideki Kakisawa, Yuki Sada, Masayuki Uesugi, Akihisa Takeuchi, Fumihiro Wakai
Citation	Journal of the European Ceramic Society, Vol. 45, No. 16, pp. 117679
Pub. date	2025, 12
DOI	https://dx.doi.org/10.1016/j.jeurceramsoc.2025.117679
Creative Commons	Information is in the article.

Journal of the European Ceramic Society 45 (2025) 117679

Contents lists available at ScienceDirect

Journal of the European Ceramic Society

journal homepage: www.elsevier.com/locate/jeurceramsoc

Strength-limiting defects evolved from heterogeneities during the sintering of high-purity submicron alumina powder

Gaku Okuma [a,*], Tsukasa Shimizugawa [b], Shingo Ozaki [b], Toshio Osada [a], Shingo Machida [c], Yutaro Arai [d], Ryo Inoue [e], Hideki Kakisawa [a], Yuki Sada [f], Masayuki Uesugi [f], Akihisa Takeuchi [f], Fumihiro Wakai [a]

[a] Research Center for Structural Materials, National Institute for Materials Science (NIMS), Ibaraki 305-0047, Japan
[b] Division of System Research, Faculty of Engineering, Yokohama National University, Tokiwadai 79-5, Hodogaya-ku, Yokohama 240-8501, Japan
[c] Materials Research and Development Laboratory, Japan Fine Ceramics Center (JFCC), 2-4-1 Mutsuno, Atsuta-ku, Nagoya, Aichi 456-8587, Japan
[d] Department of Materials Science and Technology, Tokyo University of Science, 6-3-1 Niijuku, Katsushika-Ku, Tokyo 125-8585, Japan
[e] Department of Mechanical Engineering, Tokyo University of Science, 6-3-1 Niijuku, Katsushika-Ku, Tokyo 125-8585, Japan
[f] Japan Synchrotron Radiation Research Institute, JASRI/SPring-8, Kouto 1-1-1, Sayo, Hyogo 679-5198, Japan

ARTICLE INFO

Keywords:
Sintering
Synchrotron X-ray tomography
Microstructure
Defects
Fracture

ABSTRACT

The strength-limiting defects in ceramics evolve from large inhomogeneities, such as agglomerates and aggregates, in the starting powder during sintering. The synchrotron X-ray multiscale tomography (micro-CT and nano-CT) was used to observe how defects evolve from transition alumina aggregates contained in a high-purity submicron α-alumina powder during the sintering. Complex pores, consisting of mutually interconnected pore channels, developed from aggregates through transformation, particle rearrangements, and particle coarsening due to surface diffusion. Under the constraint of the matrix, a circumferential crack was formed partly along the interface between the complex pore and the matrix. The fractography revealed that the fracture origins were complex pores on the fracture surface of bending specimens. The fracture mechanical analysis was conducted to show that both the elliptical crack model and the pore-crack model can explain the mechanical strength.

1. Introduction

Powder agglomerates, especially hard, strongly bonded ones known as "aggregates," are often found in powders produced through high-temperature processes. In ceramic powders, aggregates cause porosity inhomogeneities in the green compact [1], leading to large voids that persist in the sintered body and prevent achieving full density [2]. These voids are frequently the primary strength-limiting flaws in ceramics [3]. Therefore, the overall quality of a ceramic powder often depends largely on its aggregation state. Aggregates and inclusions in a green body represent compact inhomogeneities. When an inhomogeneity densifies at a greater rate than that of the matrix, large crack-like internal voids are formed along the inhomogeneity/matrix interface, as schematically indicated in Fig. 1(a) and (b) [4]. The tensile radial stress creates a circumferential crack (Fig. 1(a)), which will grow into a crack-like void as the inhomogeneity shrinks (Fig. 1(b)). By contrast, when the inhomogeneity is rigid or shrinks more slowly than the matrix, tensile hoop stress can produce radial cracks in the matrix [5,6].

A wide variety of pore morphologies can evolve from inhomogeneities. Quinn's textbook [7] summarizes various types of porous defects on the fractography of ceramics and glasses. The synchrotron X-ray microtomography observation revealed a collection of complicated pores that are mutually connected [8–11], as schematically illustrated in Fig. 1(c). Such porous structures have been found in the literature on the sintering of aggregates produced from transition alumina. Dynys and Halloran [2] reported complicated pore structures in sintering alum (ammonium aluminum sulfate)-derived alumina powder. Kitayama and Pask [12] showed micrographs of complex pores in the sintering of alum-derived high-purity alumina. Danzer [13] identified a fracture origin with a crescent-shaped pore surrounding a hard agglomerate in an alumina. A compact porous defect in Fig. 1(c) is classified by its connectivity or genus *g*. Roughly speaking, it is the number of holes in the pore surface. A spherical pore is characterized as a genus-zero surface. A doughnut-shaped pore (torus) has genus one.

* Corresponding author.
E-mail address: Gaku@nims.go.jp (G. Okuma).

https://doi.org/10.1016/j.jeurceramsoc.2025.117679
Received 24 February 2025; Received in revised form 1 May 2025; Accepted 15 July 2025
Available online 16 July 2025

Okuma [8–10] termed the mutually interconnected pore with $g > 0$ as a complex pore.

A high-purity and submicron alumina, produced by the hydrolysis of aluminum alkoxide [14], has been widely used commercially and as the model material for investigating the relationship among sintering, microstructure, and mechanical strength. Su and Johnson [15] proposed the concept of the master sintering curve based on the experimental results of sintering this alumina powder. Ozaki and co-workers [16] developed a finite element analysis methodology to predict stochastic fracture behavior based on the size and shape of large defects observed by scanning electron microscopy and X-ray computed tomography (X-ray CT). They analyzed the material made by sintering the same alumina powder used by Su and Johnson. Here, we studied the microstructure of Ozaki's model material using synchrotron X-ray multiscale tomography and revealed how complex pores evolved from aggregates produced from transition alumina during sintering. The circumferential cracks between the complex pore and the matrix in Fig. 1(d) may be the strength-limiting defects.

As aggregates and inclusions are detrimental to the sintering process, treatments such as classification, sieving, filtering, or milling and grinding, which aim to remove larger ones, can significantly enhance sintering performance [2]. The reliability of ceramics can be greatly increased by dispersing the powder in a liquid and filtering the suspension to remove strength-degrading heterogeneities prior to forming engineering shapes [17,18]. However, it is impossible to remove every aggregate smaller than a few microns. Even in various high-purity submicron alumina powders, complex pores smaller than 10 microns have been found to remain in sintered bodies [8–10]. Structures resembling complex pores can evolve from aggregates in many submicron ceramic powders, such as submicron zinc oxide (ZnO) powder [11]. In multilayered structures, such as those used in electronic devices, where layers can be just a few microns thick or less, even minute defects can significantly impact electrical performance. In this study, we conducted a detailed analysis of how large aggregates evolve into complex pores. The knowledge obtained here will be useful for alumina and improving the reliability of many other ceramic materials.

2. Experimental

2.1. Starting material

The powder used in this study was high-purity (99.99 %) α-alumina (Al_2O_3) (AKP-50, Sumitomo Chemical Co., Ltd.), synthesized via hydrolysis of aluminum alkoxide followed by calcination. During calcination, hydrated alumina (e.g., boehmite) typically transforms through γ-, δ-, and θ-Al_2O_3 before reaching the thermodynamically stable α-phase at high temperatures [14]. The impurity concentration of AKP-50 is Si 10 ppm, Na 3 ppm, Mg 2 ppm, Cu 1 ppm, and Fe 1 ppm. The powder consisted of primary α-alumina particles ranging from approximately 0.1 to 0.3 μm (Fig. 2(a)). The powder contained aggregates with different shapes and sizes that were supposed to be residual transition alumina that had not been fully converted to α-alumina. The small

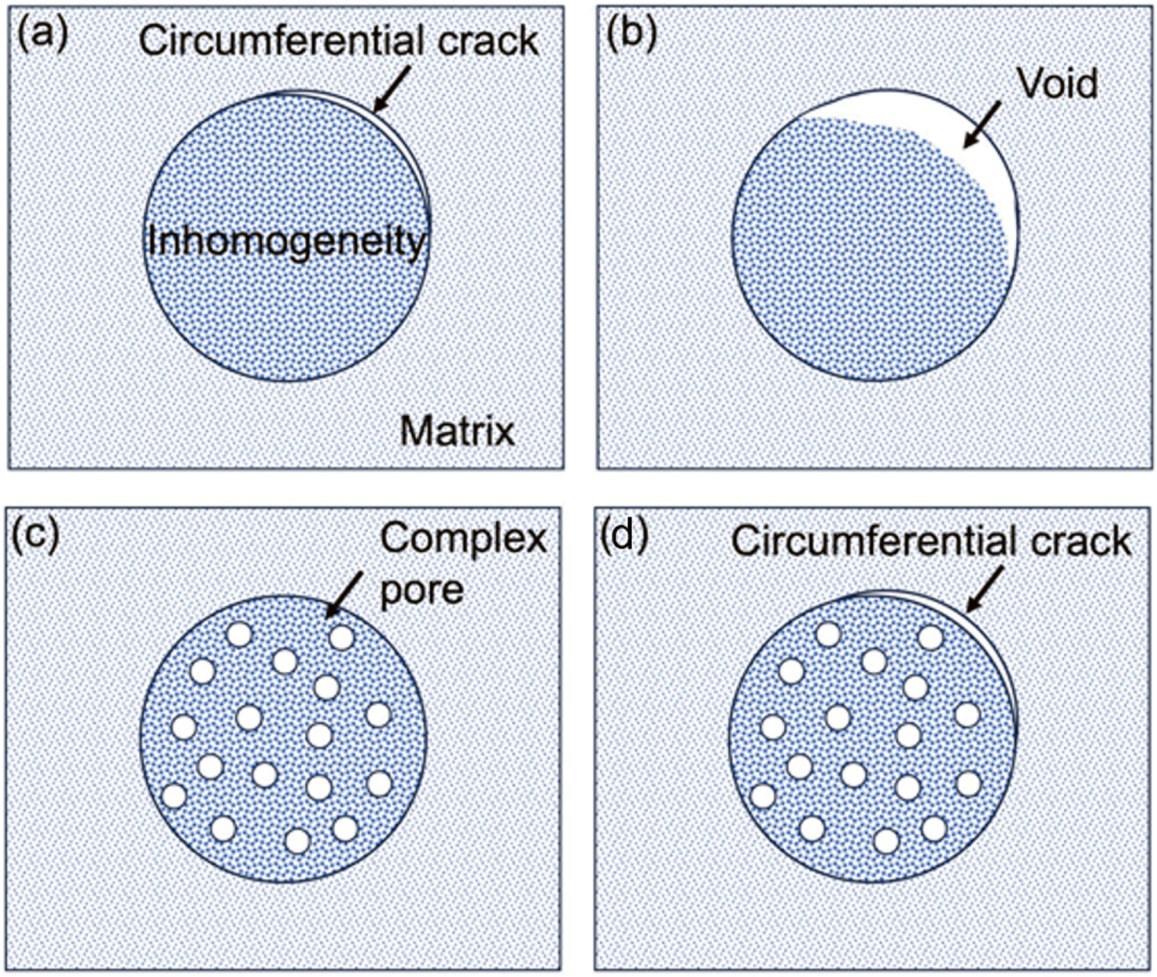

Fig. 1. Formation of strength-limiting defects. (a) formation of a circumferential crack between the matrix and the rapidly shrinking inhomogeneity, (b) enlargement of the circumferential crack to form a large void, (c) formation of a complex pore from a transition alumina aggregate, (d) formation of a circumferential crack between the matrix and the complex pore.

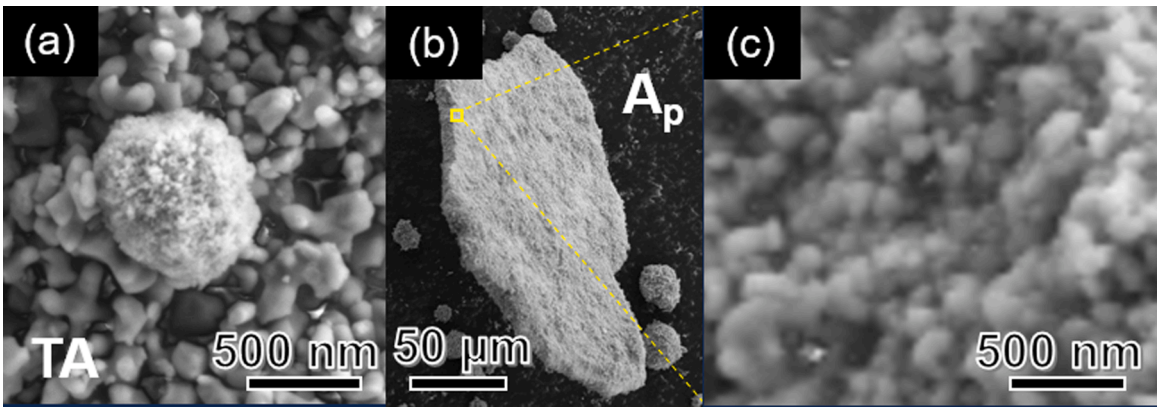

Fig. 2. SEM image of AKP-50 alumina powder. (a) primary α-alumina particles with particle sizes from 0.1 to 0.3 μm on the surface of an agglomerate. A small transition alumina aggregate at the center is an unreacted phase. (b) plate-like agglomerate, (c) magnified view of the square in (b).

aggregate at the center of Fig. 2(a) consisted of nanocrystalline particles. We refer to them as transition alumina aggregates. When viewed at low magnification, the as-received powder formed irregularly-shaped agglomerates, including plate-like ones (Fig. 2(b)). The magnified view of the plate-like agglomerate in Fig. 2(c) shows that it consists of primary α-alumina particles, the same as Fig. 2(a). Although it is a common practice to remove large aggregates, we sintered the as-received powder to investigate how defects evolved from them.

2.2. Sample preparation

The as-received powder was initially compacted by uniaxial pressing at 51 MPa for 3 min, followed by cold isostatic pressing (CIP) at 100 MPa for 3 min. The packing density of the green body was determined based on the sample dimensions, yielding a value of 54.6 %. The pressureless sintering of powder compacts with a diameter of 20 mm and a thickness of 4 mm was carried out in air at 1400, 1500, and 1600 °C for 2 h, using heating and cooling rates of 200 °C/h. The resulting samples exhibited relative densities ρ of 97.6 %, 98.4 %, and 98.9 %, respectively. A sample with ρ of 62.8 % (measured by the Archimedes method) was also prepared by the pressureless sintering of a powder compact at 1150 °C for 1 h to observe the initial packing structure.

Cylindrical samples with a diameter of 0.85 mm were fabricated by laser beam machining for X-ray CT observation. Laser cutting was performed using a Nd:YAG pulsed laser with a wavelength of 1064 nm. A beam diameter of 30–40 μm was selected to minimize damage to the sample.

2.3. X-ray CT measurements and image analysis

The synchrotron X-ray CT experiments were performed at beamline BL20XU of the Japanese synchrotron radiation facility, SPring-8, utilizing an X-ray energy of 20–30 keV for both micro-CT and nano-CT modes [19,20]. The micro-CT mode employed simple X-ray projection optics, utilizing absorption contrast for imaging. In contrast, the nano-CT mode utilized a more complex optical system comprising a phase contrast X-ray full-field microscope. This system included components such as a hollow-cone illumination setup (using a condenser zone plate (CZP)), sample stages, a Fresnel zone plate (FZP) objective, a Zernike phase plate (phase ring), and a visible-light conversion type X-ray image detector. Given that the phase-shift cross section in the X-ray region can be up to a thousand times larger than that of absorption, phase contrast X-ray imaging was used to achieve highly sensitive observations of fine structures. Samples were rotated in 0.1° increments up to a total of 180°. The voxel sizes for the micro-CT and nano-CT modes were 0.5 μm and 33–42 nm, respectively. The measurement time for each sample was 8 min for micro-CT, and 30 min for nano-CT when observing a region of interest within the sample. 3D visualization and geometrical measurements were carried out using Amira software (VSG, Burlington, MA). Gaussian filtering was applied to reduce noise in the 2D images, and a local thresholding method was utilized to segment the gray value images into pores and material for defect size measurement. The surfaces were discretized using triangular meshing, allowing for the calculation of the volume and surface area of the defects.

2.4. Bending test

A four-point bending test was conducted at room temperature with a span length of 16 mm. The crosshead speed was maintained at 0.5 mm/min. The bending strength σ_f was calculated using the following equation:

$$\sigma_f = \frac{3P(L_1 - L_2)}{2bt^2} \quad (1)$$

where P represents the maximum bending load, L_1 (= 30 mm) is the span length of outer supports, L_2 (= 10 mm) is the span length of inner supports, b (= 4 mm) is the specimen width, and t (= 3 mm) is the specimen thickness. The surfaces of the specimens were mirror-polished, and the test method conformed to the Japanese Industrial Standard (JIS R 1601). In this investigation, bending tests were carried out on samples sintered at 1500 °C [16].

2.5. SEM observations and image analysis

The two-dimensional (2D) microstructural characteristics of sintered alumina were investigated using field emission scanning electron microscopy (FE-SEM, ZEISS GeminiSEM 300, Germany) equipped with electron backscatter diffraction (EBSD) capabilities. Both the polished cross-sectional microstructure and the fracture surfaces were observed. Grain size was determined by measuring the diameter of equivalent circles derived from EBSD maps, using TSL OIM analysis software.

3. Results

3.1. Initial packing structure

3.1.1. CT observation of initial packing

The heterogeneous packing structure of the powder compact calcined at 1150 °C (ρ = 62.8 %) is observed in a slice from the reconstructed micro-CT images (Fig. 3). In micro-CT, image contrast is generated by differences in X-ray absorption coefficients, enabling visualization of the particle packing density distribution [8].

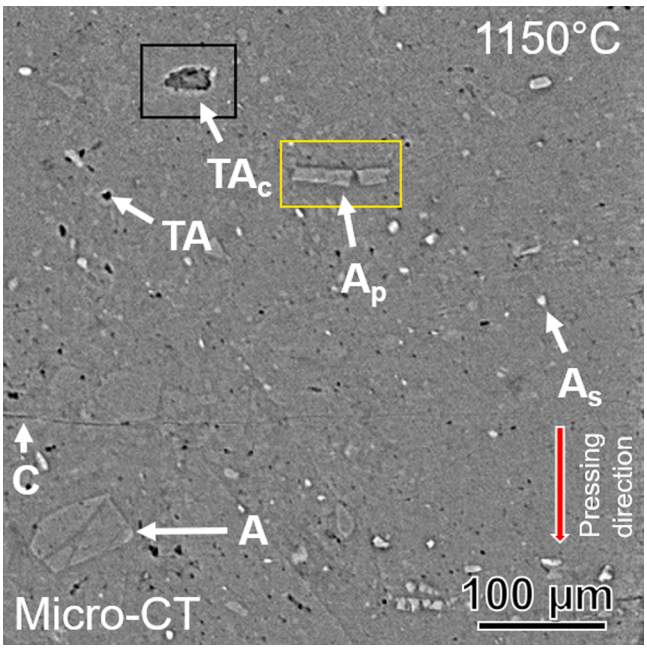

Fig. 3. Initial packing structure (density = 62.8 %, calcined at 1150°C) observed by micro-CT. Various types of agglomerates and transition alumina aggregates were found in the calcined body. A: Agglomerate, A_p: Agglomerate (Plate-like), A_s: Small agglomerate, TA: Structure evolved from transition alumina aggregate, TA_c: Composite structure evolved from transition alumina aggregate, C: Crack.

High-density regions appear brighter, while low-density regions appear darker. Angular-shaped agglomerates are observed as brighter, densely packed regions (A), with some agglomerates displaying a plate-like shape (A_p). Small round agglomerates looked white (A_s). A thin crack indicated by the arrow (C) is believed to have been formed during handling, as the calcined body is fragile. Various objects are observed as darker, loosely packed regions in Fig. 3, as indicated by symbols for a small one (TA) and a large composite structure (TA_c). We suppose they are structures evolved from transition alumina aggregates originally included in the as-received powder, like that shown in Fig. 2(a), although they differ in size.

Fig. 4 presents a nano-CT image of the composite structure (TA_c) enclosed by the black square in Fig. 3. Slight variations in particle packing density can be sensitively detected by nano-CT utilizing phase shift. The nano-CT image reveals that the darker, loosely packed region is not homogeneous but has an inhomogeneous density distribution, containing several substructures inside. For example, an elongated substructure (E) is included in this region. The nano-CT image demonstrates a lower packing density along the interface between this region and the matrix.

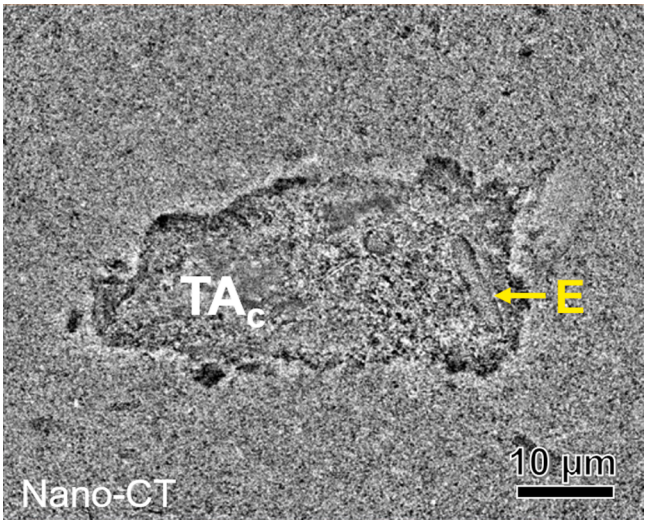

Fig. 4. Enlarged view of a darker, large composite structure evolved from transition alumina aggregate (TA_c), located in the area enclosed by the square in Fig. 3(a), as observed by nano-CT. (E) indicates the elongated structure.

The particle morphologies of different transitional alumina phases range from fibers and rods to platelets through transformation occurring during the heat treatment [21]. The composite structure suggests that large transitional alumina aggregates consist of particles of different phases and morphologies that remained in the as-received powder. This may explain why this region appears structurally modified at 1150 °C relative to the surrounding α-alumina matrix. In particular, the rod-like structures, also seen in Fig. 4 (indicated by arrow (E)), might reflect a domain of transitional phases that had not fully converted to α-alumina in the as-received powder.

3.1.2. SEM observation

Various types of defects and agglomerates were observed by SEM on the polished cross-section of the sample with a relative density of 62.8 %, as shown in Fig. 5. The porous object in Fig. 5(a) is composed of fine particles smaller than the primary particles in the matrix. It corresponds to the structure evolved from transition alumina aggregate (TA) in Fig. 3, which looks like a void when observed by micro-CT. SEM observation revealed that the structure (TA) evolved from transition alumina aggregates. Furthermore, Fig. 5(b) corresponds to the complex structure (TA_c) observed in Fig. 3 and Fig. 4. This structure consists of fine particles and rod-like substructures. The structure observed in Fig. 5 (c) corresponds to a small white structure (A_s) in Fig. 3 and is identified as a small agglomerate more densely packed than the surrounding matrix. From Fig. 5(c), it is confirmed that this small agglomerate is composed of primary particles.

3.2. Microstructural evolution during sintering

3.2.1. Grain growth in the matrix and complex pores

The microstructures of sintered alumina were imaged by EBSD in the previous report [16]. Grain sizes in the matrix increased with temperature: 2.8, 3.8, and 5.4 μm at 1400, 1500, and 1600 °C, respectively. Fig. 6 shows SEM micrographs of large defects on the polished surfaces of specimens sintered at 1400–1600 °C. Although these large defects resemble voids or cavities, the high-magnification images in Fig. 6(d)-(f) reveal porous structures of particles smaller than the matrix grains. Numerous circular contact marks were observed on the surfaces of the particles. This observation suggests that partially sintered porous regions—i.e., complex pores—were detached partly from the matrix during polishing, resulting in the formation of voids. The magnified images show that the particle sizes within the defects at 1400, 1500, and 1600 °C were approximately 0.8, 1.4, and 2.8 μm, respectively. These sizes are smaller than those in the surrounding matrix, likely due to the inhibition of grain growth within the porous structure.

3.2.2. Coarsening of complex pores

X-ray CT enables us to observe the evolution of complex pores and other defects non-destructively, providing a more accurate view of internal porous structures without damage caused by polishing the cross-section. Because of resolution limitations, micro-CT images showed complex pores as voids (Fig. 7(a)-(c)). The comparison with the initial packing structure in Fig. 3 indicates that the complex pores are developed from the structures evolved from transition alumina aggregates TA and TA_c. With the higher resolution of nano-CT (Fig. 7(d)-(f)), it became clear that these complex pores are filled with particles. This porous structure looks like porous colonies of α-alumina consisting of grains with an interconnected wormy morphology. The morphology of

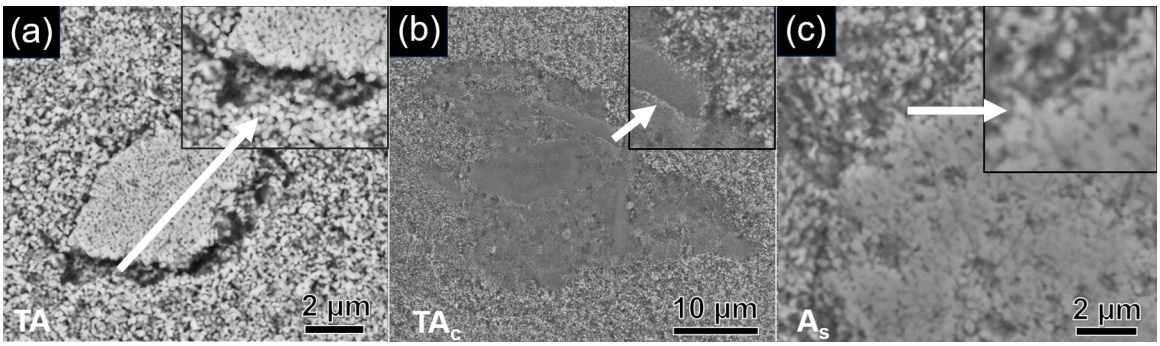

Fig. 5. SEM image of (a) a structure (TA) evolved from transition alumina aggregate, (b) a large composite structure (TA_c) evolved from transition alumina aggregate, (c) small white agglomerates (A_s) in the calcined body (ρ = 62.8 %).

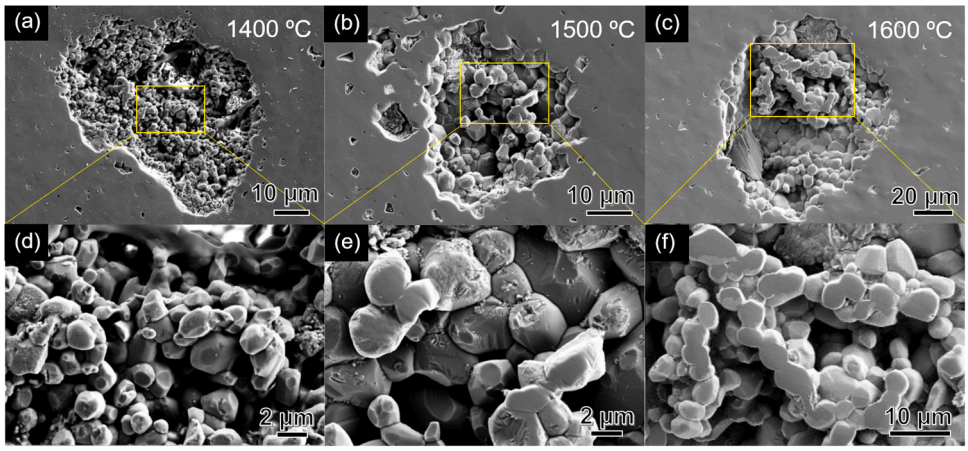

Fig. 6. Cross-sectional SEM image of complex pore in the specimen sintered at (a) 1400 °C (relative density, ρ = 97.6 %), (b) 1500 °C (ρ = 98.4 %), (c) 1600 °C (ρ = 98.9 %).

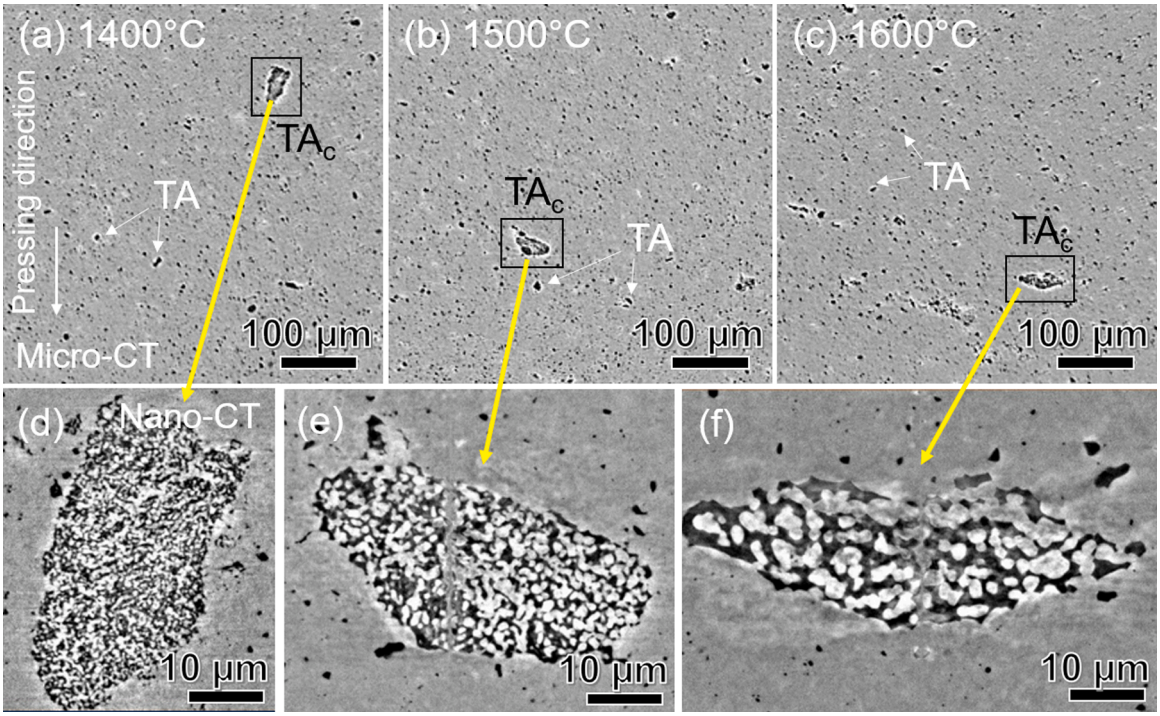

Fig. 7. Micro-CT images of microstructures of alumina sintered at (a) 1400°C, (b) 1500°C, and (c)1600°C (TA: structure evolved from transition alumina aggregate, TA_c: composite structure evolved from transition alumina aggregate). Magnified view of complex pores observed by nano-CT. (d) 1400°C, (e) 1500°C, and (f)1600°C. The complex pores exhibit structures containing numerous particles inside rather than mere cavities.

α-alumina particles is similar to the vermicular particles characteristic of aggregates derived from transition alumina [22].

The 3D reconstruction of complex pores is illustrated in Fig. 8. The alumina phase is shown in the solid view, while the pore phase is displayed in the pore view. The solid/pore two-phase system has a bicontinuous and interpenetrating structure resembling nanoporous materials, such as nanoporous metals [23,24]. Although the microstructure evolved drastically with temperature, the solid volume fraction was almost constant, probably because the surrounding matrix constrained the shrinkage of the complex pore. The relative density within complex pores remained nearly constant at approximately 0.5 between 1400 and 1600 °C. The total surface area A_{pore} in the unit volume V (13 ×13 ×13 μm^3) was measured from the 3D structure of complex pores. The specific surface area $S_V = A_{pore}/V$ decreased with increasing sintering temperature in Fig. 9. It shows that the microstructural evolution of complex pore occurs toward decreasing the total surface area.

The microstructures observed in the pore view in Fig. 8 indicate the coarsening of the pore network structure. Understanding this coarsening process is important, since the microstructure of a complex pore should affect its mechanical response. Whereas grain growth occurs by grain boundary migration, coarsening of bicontinuous porous structures occurs by surface motion due to surface diffusion driven by the gradient of chemical potential, which is proportional to surface free energy and surface curvature [25]. While grain growth, discussed in the previous section, is defined based on grain boundaries, the coarsening of a porous material can be defined based on the interface between the solid space and the pore space, i.e., the surface [26,27]. For the cross-section of complex pores in Fig. 7(d)-(f), the mean intercept length (l_{MIL}) is measured by counting the number of intersections between the solid/-pore interface and a set of parallel lines. The value of l_{MIL} is derived from the total line length L and the number of intersections n:

$$l_{MIL} = L/n \tag{2}$$

Fig. 10 demonstrates that the mean intercept length increases with increasing sintering temperature. This is the coarsening, a characteristic of the evolution of porous structure commonly observed when the densification is suppressed [23]. The mean intercept length can be divided into components corresponding to the solid phase and the pore phase as follows:

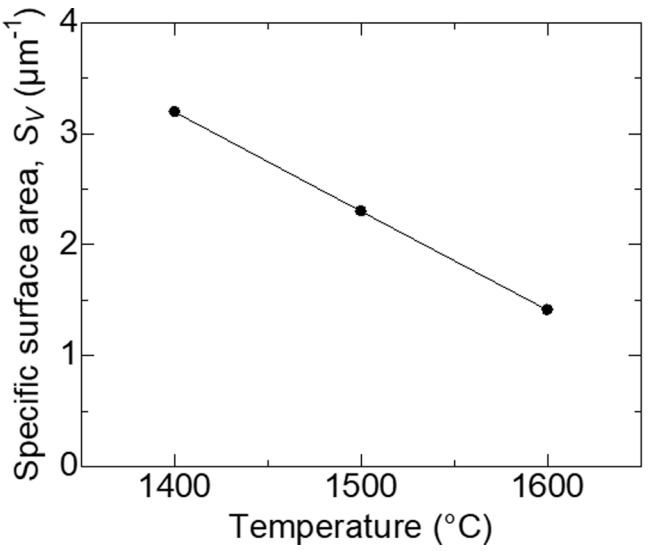

Fig. 9. Specific surface area plotted as a function of sintering temperature.

$$l_{solid} = 2\rho l_{MIL} \tag{3}$$

$$l_{pore} = 2(1\text{-}\ \rho)\ l_{MIL} \tag{4}$$

where ρ is the relative density of the complex pore. The value of l_{solid} is associated with the mean size of the solid phase. The increase of l_{pore} is referred to as pore coarsening. Since the relative density of the complex pore is approximately 0.5 and does not vary during the densification of the matrix phase, both l_{solid} and l_{pore} increase with densification. Thus, the formation process of complex pores occurs by domain coarsening and pore coarsening under conditions where the surrounding matrix constrains shrinkage.

The mean intercept length in a complex pore is also determined by the specific surface area according to quantitative stereology [28]:

$$l_{MIL} = 2/S_V \tag{5}$$

The mean intercept length calculated by the specific surface is also plotted in Fig. 10. It agrees with the value measured by Eq. (2) approximately. The increase in the intercept length is a natural consequence of the specific surface area of the complex pore decreasing with

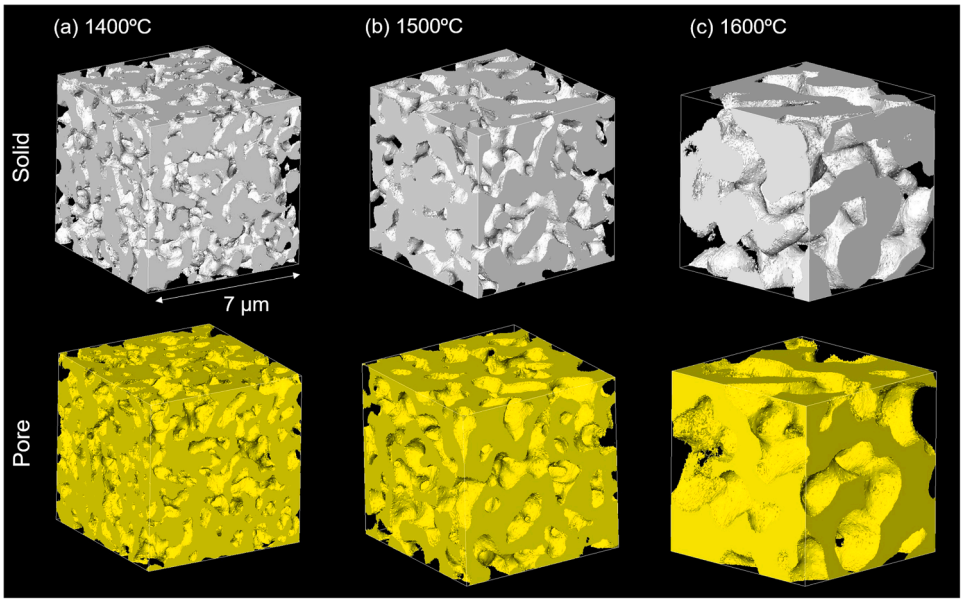

Fig. 8. 3D solid and pore structures within complex pores at (a) 1400°C, (b) 1500°C, and (c) 1600°C.

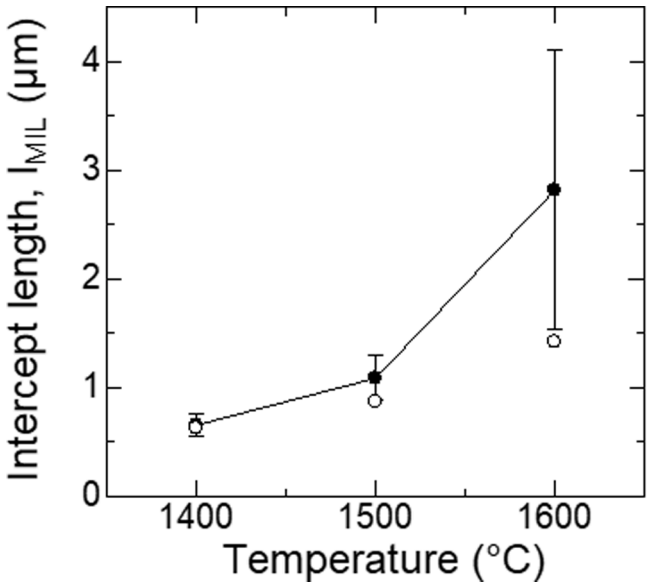

Fig. 10. Microstructural coarsening within the complex pore during sintering. Filled circles show mean intercept length (l_{MIL}), plotted as a temperature function. Open circles show $2/S_V$.

increasing temperature.

3.2.3. Topological evolution of complex pore

The complicated porous structure of the complex pore in Fig. 8 is characterized by the Euler characteristic, which is related to the genus g [29]. The genus is the number of holes in the pore surface in Fig. 8. For a porous structure composed of N pores, the total Euler characteristic is expressed as:

$$X = \sum_{n=1}^{N}(2-2g) \tag{6}$$

The total Euler characteristic is obtained from the nano CT images by using the Gauss-Bonnet theorem

$$X\Big/2 = \frac{1}{4\pi}\int_A KdA \tag{7}$$

where $K = \kappa_1\kappa_2$ is the Gaussian curvature. The normalized Euler characteristics per unit volume V is given as

$$X/V = \overline{K}S_V/2\pi \tag{8}$$

where $\overline{K}$ is the average Gaussian curvature. X/V is calculated from the CT images (Fig. 8) and is plotted as a function of relative density in Fig. 11. The monotonic increase in the Euler characteristic observed during sintering indicates a corresponding decrease in the genus as sintering progresses. The relationship between Euler characteristics and the topological evolution of porous structure will be discussed in 4.1.

3.3. Complex pores as fracture origins

The circumferential cracks between the complex pore and the matrix will be fracture origins. In the 2D cross-sectional nano-CT image (Fig. 12 (a)), gaps between a complex pore and the matrix, indicated by white arrows, were observed. Fig. 12(b) presents a 3D reconstruction of a complex pore, revealing that the gap is a circumferential crack. Since this crack extends for tens of micrometers, it may be considered a defect that could potentially influence the fracture behavior of the ceramic.

Figs. 13 and 14 show fracture origins found on fracture surfaces of specimens sintered at 1500 °C, tested under four-point bending (The positions of the defects shown in Fig. 13 and Fig. 14 within the entire specimens are presented in Supplementary Fig. S1 and Fig. S2, respectively). The specimen with the lowest strength, 248 MPa, fractured from a large complex pore at the tensile side. In Fig. 13, both halves of the fracture surface are presented: (a) shows the fracture surface containing the complex pore, while (a') displays the fracture surface with a void where the complex pore was removed partly. The comparison between areas in the red square in (a) and the blue square (a') indicates that the fracture occurred along the circumferential crack between the complex pore and the matrix. The crack pattern was complicated, so the branched crack propagated inside the complex pore (upper-left in (a')).

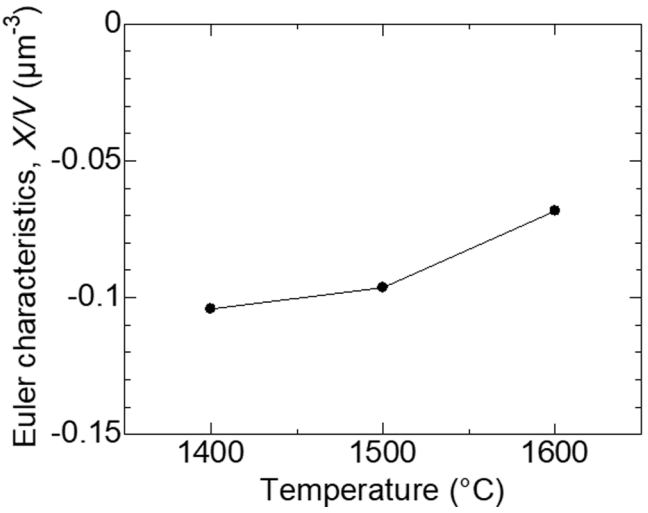

Fig. 11. Euler characteristics plotted as a function of sintering temperature.

In contrast, the specimen with the highest strength, 368 MPa, fractured from a smaller internal complex pore in Fig. 14. The lower edge of (a) was the tension surface, and the fracture origin was located 10 μm from the specimen surface. Both halves of the fracture surface are presented in Fig. 14: (a), (b), and (c) show the fracture surface containing the complex pore, while (a'), (b'), and (c') display the fracture surface with a void where the complex pore was removed. The crack propagated along the interface between the complex pore and the matrix. Circular contact areas were observed on some particles of the complex pore (c) and grains of the matrix wall (c'). These contacts partly bridged the complex pore and the matrix. The fracture occurred by breaking these contact areas.

3.4. Defects generated from plate-like agglomerates

Large defects were also found at the interface between a rectangular structure and the matrix, as shown in Fig. 15(a). This rectangular structure is presumably developed from a plate-like agglomerate in the as-received powder (Fig. 1(b), (c)) and corresponds to the structure A_p observed in the initial packing structure (Fig. 3). Although the rectangular structure contained several dark areas, the size and the number of dark areas per unit area were much smaller than those in the matrix. The plate-like agglomerate in the as-received powder shrinks faster than the matrix region at 1400°C, then forms a dense rectangular structure. Fig. 15 (b) illustrates the 3D structure of the defect along the boundary of the plate-like structure. It has a crack-like feature and can be a strength-limiting defect. Crack-like structures at the boundary of such plate-like agglomerates were previously observed in a material prepared by sintering a submicron alumina powder (TMDAR) [9].

4. Discussions

4.1. Evolution of complex pore

The strength-limiting complex pores should be developed from

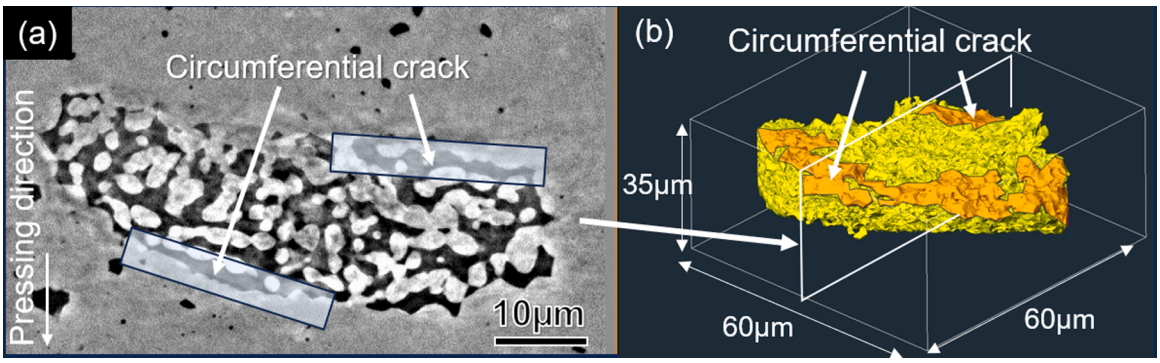

Fig. 12. (a) 2D cross-sectional nano-CT image (1600 °C). (b) 3D reconstruction of a complex pore. The arrows indicate a gap (circumferential crack) between the complex pore and the matrix.

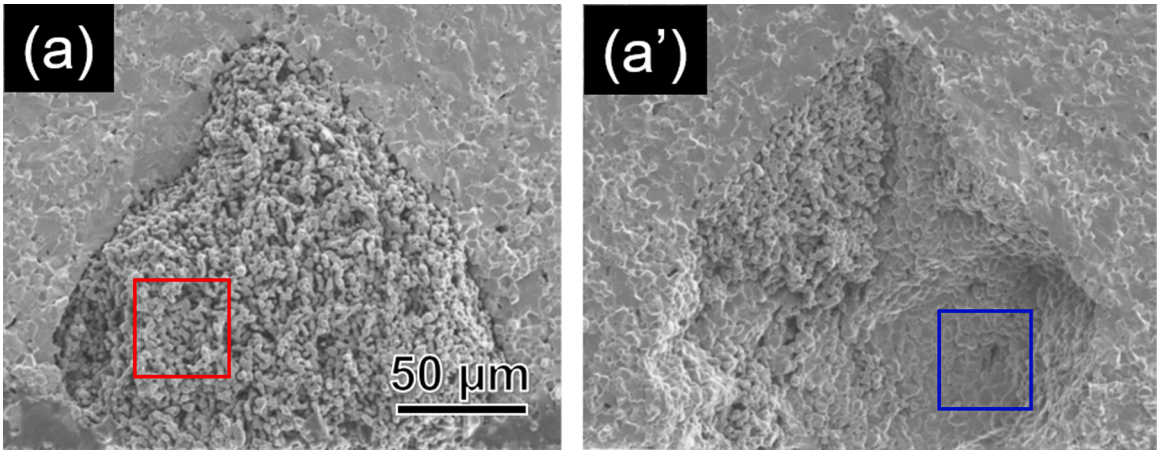

Fig. 13. SEM images of the fracture surface of a specimen with the lowest strength (248 MPa). The bottom edge of the SEM image is the tensile surface of the bending specimen. (a) fracture surface containing the complex pore and (a') fracture surface with a void where the complex pore was removed partly.

transition alumina aggregates included in the as-received powder. Legros [30] studied the phase transformation and densification of nanocrystalline γ-alumina. The diffusive γ-α transformation involves nucleation of the α phase, rearrangement of the γ crystallite at the α seed and grain surface, and formation of porous α alumina monocrystalline colonies. The γ-α transformation completes at 1100 and 1180 °C at 1 °C/min and 10 °C/min, respectively. The α alumina particles derived from transition alumina are typically wormy [22]. The complex pore forms porous networks of fine α-alumina grains, schematically illustrated in Fig. 16. Although the shrinkage of porous structure is constrained by the matrix, the volume of a particle changes by surface diffusion at elevated temperatures. Consider a small particle bridging two larger particles in Fig. 16. Atoms on the smaller particle will diffuse toward the larger particles on both sides. As the smaller particle shrinks, the contact radius decreases with time, and finally, the bridge will be broken by pinch-off. The pore coarsening will occur due to the coalescence of pore channels, which were initially separated by the bridge. The successive occurrence of pinch-offs causes the pore coarsening. As the number of pore channels is topologically related to genus and Euler characteristics, the pinch-off events and pore coarsening can be monitored using Euler characteristics.

4.2. Fracture strength

4.2.1. Elliptical crack model

The nano-CT revealed that a circumferential crack is partly formed along the interface between the complex pore and the matrix, as illustrated in Fig. 12 (b). The fractographic observation indicated the fracture occurred along the circumferential crack in Figs. 13 and 14. The exact fracture mechanics analysis of these fracture origins is impossible due to their complex shape. However, as the first step, we assume the circumferential crack can be modeled by an elliptical internal crack subject to far-field tension stress (Fig. 17 (a)) or a semi-elliptical surface crack under bending (Fig. 17(b)). For elliptical or semi-elliptical cracks, the stress intensity factor acting on the flaw is [31]:

$$K_I = Y\sigma\sqrt{a} \tag{9}$$

and fracture occurs when:

$$K_{Ic} = Y\sigma_f\sqrt{a} \tag{10}$$

where K_{Ic} is the fracture toughness, σ_f is the fracture stress at the origin location, a is a measure of the origin size (e.g., depth for a surface crack in Fig. 17). The stress intensity shape factor Y is a dimensionless parameter that is a function of the shape and size of the crack.

Newman and Raju [32] expressed the stress intensity factor K at any point along the crack front in a finite thickness plate and beam in Fig. 17. Their results are expressed by using the stress intensity shape factor Y in Eq. (9).

For embedded elliptical cracks (volume origin in Fig. 17(a)) under remote tensile stress:

$$Y = \sqrt{\pi/Q}F_e(a/c,\quad a/t,\quad c/b',\phi) \tag{11}$$

For semi-elliptical surface cracks (surface origin in Fig. 17(b)) under remote bending stress:

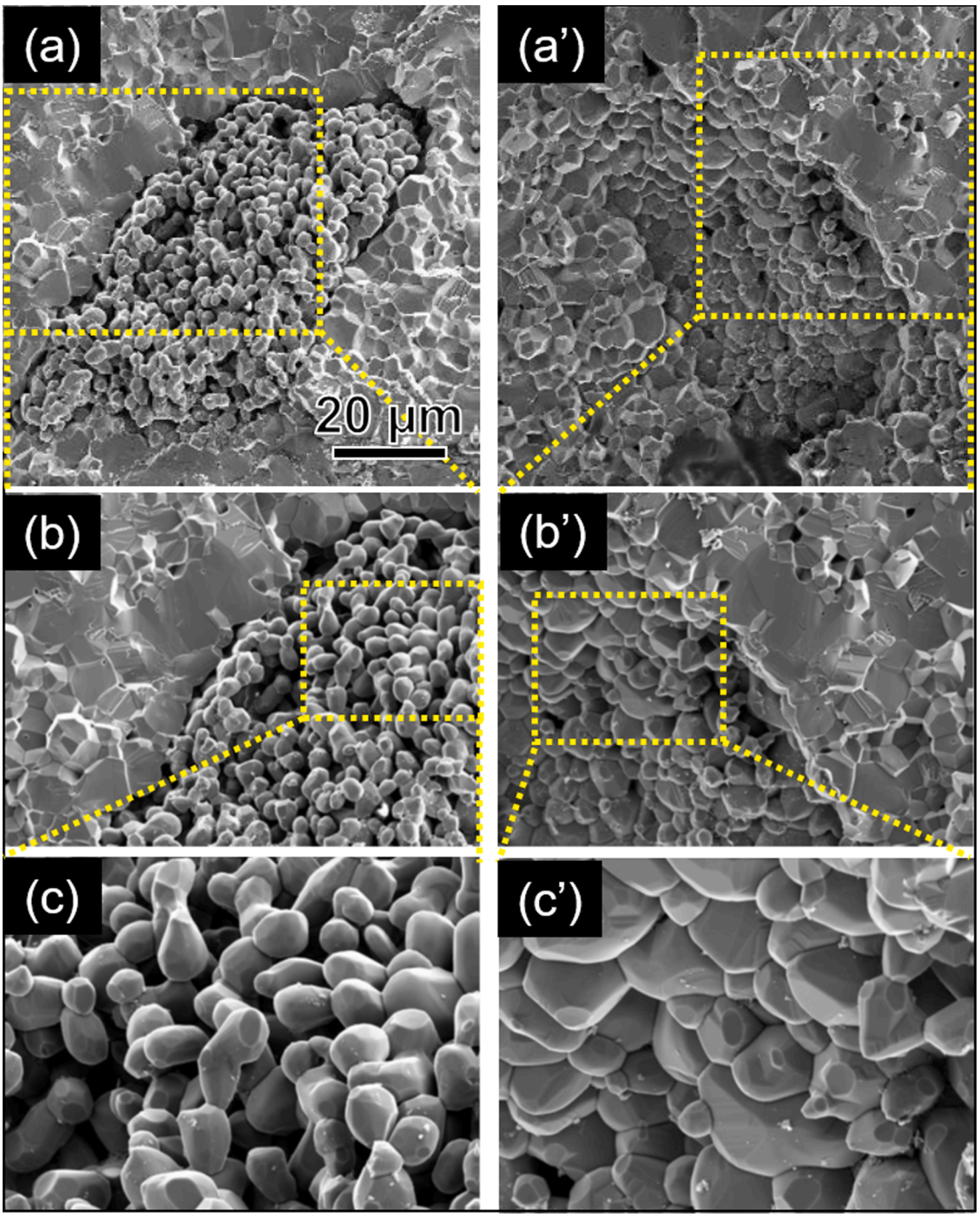

Fig. 14. SEM image of the fracture surface of a specimen with the highest strength sample (368 MPa). The fracture originated from a volume origin within the sample. (a), (b), (c) fracture surface containing the complex pore, and (a`), (b`), (c`) fracture surface with a void where the complex pore was removed.

$$Y = \sqrt{\pi/Q} H_s F_s(a/c, a/t, c/b', \phi) \tag{12}$$

where the function Q is the shape factor for an ellipse and is given as a function of the aspect ratio a/c, the boundary correction factors F_e and F_s are functions of c/a, the ratio of crack depth to specimen thickness a/t, the ratio of crack width to the specimen width c/b', and the parametric angle ϕ. The bending multiplier H_s is a function of a/c, a/t, and ϕ. The stress intensity factor varies with the position along the elliptical crack front. The position on the crack periphery is described by the parametric angle ϕ in Fig. 17(c) for c/a less than unity. For semi-elliptical surface cracks, Eq. (12) is applicable for $0.5 < c/a < \infty$. The fracture of small semi-elliptical surface cracks is classified into three groups according to the aspect ratio c/a: (i) the maximum stress intensity factor appears at the surface ($\phi = 0$) for $c/a < 1$, (ii) the maximum stress intensity factor appears at the crack depth ($\phi = \pi/2$) for $c/a > 1$, (iii) the stress intensity factor at the surface is almost the same with that at the crack depth for $c/a = 1$. For embedded defects of volume origin, the maximum stress intensity factor arises at the minor semi-axis of the elliptical crack.

We approximated fracture origins, for example, in Fig. 13 or Fig. 14, by semi-elliptical surface cracks or embedded elliptical cracks, respectively. Fig. 18 shows the observed bending strength is approximately proportional to $1/Y\sqrt{a}$, where the quantity is calculated from the shape and size of complex pores. The fracture stresses of the weakest specimen (Fig. 13) and the strongest specimen (Fig. 14) are indicated as blue circle

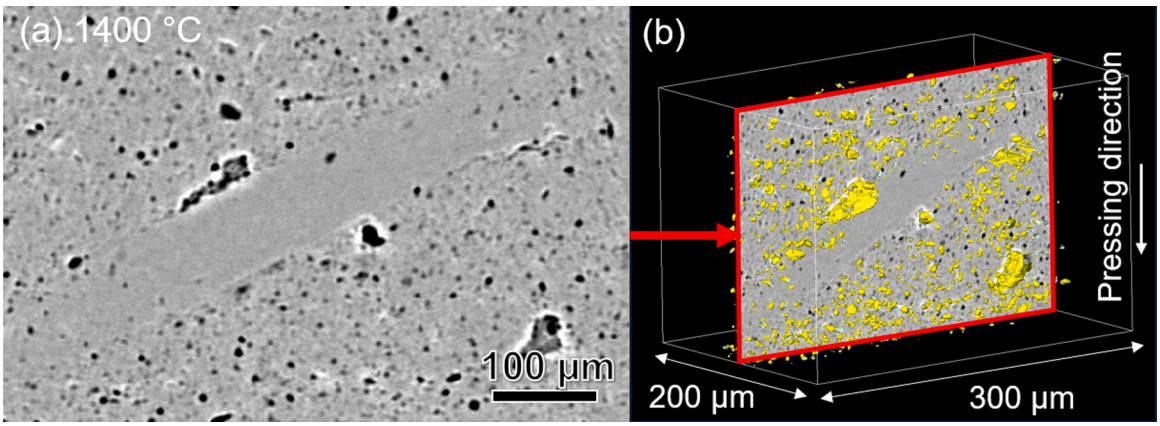

Fig. 15. (a) Defects around a structure developed from a plate-like agglomerate observed by micro-CT. (b) 3D defects along the boundary of a plate-like structure.

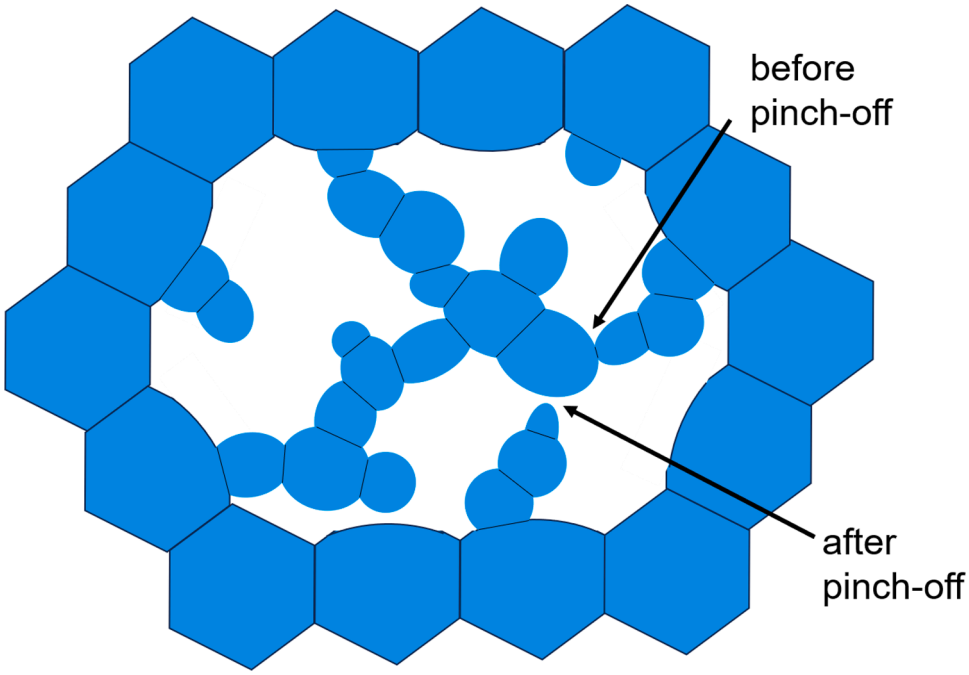

Fig. 16. Schematic illustration of solid-phase pinch-off and pore coarsening during constrained sintering, where the surrounding matrix confines a porous defect composed of interconnected small α-alumina particles. The pinch-off of the solid phase leads to the coalescence of pore channels, resulting in pore coarsening.

and red triangle, respectively. The slope of lines in Fig. 18 gives the fracture toughness K_{Ic}. The estimated fracture toughness of surface crack ranged from 2.7 MPa·m$^{1/2}$ (group (i), $c/a < 1$) to 3.3 MPa·m$^{1/2}$ (group (iii), $c/a = 1$). The real circumferential cracks, however, cover the complex pore partly, and the initial crack plane may not be perpendicular to the tensile axis. The actual size and orientation of circumferential cracks cannot be determined only from the shape and size of complex pores. Therefore, it is quite natural that the apparent fracture toughness of a specimen is different from that of other specimens. As the assumption of an elliptical crack overestimates the crack size, the true fracture toughness may be smaller than the apparent value.

The fracture toughness of alumina ceramics depends on grain size and test technique [33–36]. The crack resistance (R-curve) increases with crack extension due to frictional-pullout relation in a grain-bridging model [37]. The total toughness K_R is a sum of the crack tip toughness K_0 and the term $K_\mu(a)$ that depends on the crack length a and shields the crack tip from the externally applied load. Seidel and Rödel [38] reported a mean crack tip toughness of 2.3 MPa·m$^{1/2}$ for alumina, independent of grain size between 0.9 and 16 μm. The crack tip toughness was significantly lower than the toughness of 3–4 MPa·m$^{1/2}$ evaluated by indentation techniques. The apparent fracture toughness 2.7 – 3.3 MPa·m$^{1/2}$ was intermediate between the crack tip toughness K_0 and the typical value for alumina.

4.2.2. *Pore-crack model*

If a circumferential crack surrounds a complex pore perfectly, the complex pore separated from the matrix by a gap can be considered a single large pore, cavity, or void. A large pore acts as a stress concentrator, and the fracture occurs from cracks at the pore surfaces. Baratta [39] and Evans [40] analyzed pore-induced failure by considering two cases: an equatorial annular crack around a spherical pore [39,40] (Fig. 19(a)) and semicircular cracks near a spherical pore [40,41] (Fig. 19(b)). Although the annular crack is termed a “circumferential crack” in some literature, we distinguish the annular crack, which is perpendicular to the pore surface, from the circumferential crack in Fig. 1, which is parallel to the interface between the inhomogeneity and the matrix. Zimmermann [41] and Flinn [42] analyzed the fracture strength of alumina with artificial spherical pores as a function of grain

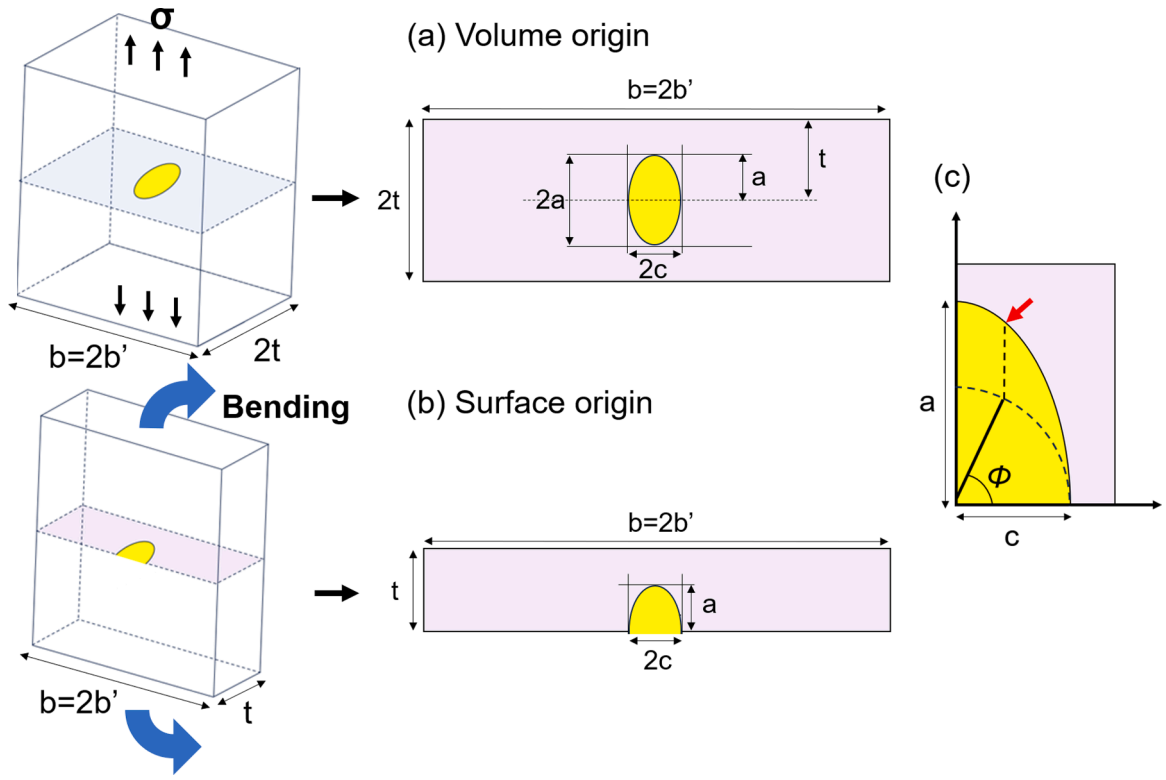

Fig. 17. (a) Internal (volume) cracks and (b) surface cracks in plates for far-field tension stresses. (c) Coordinate system used to define parametric angle [31].

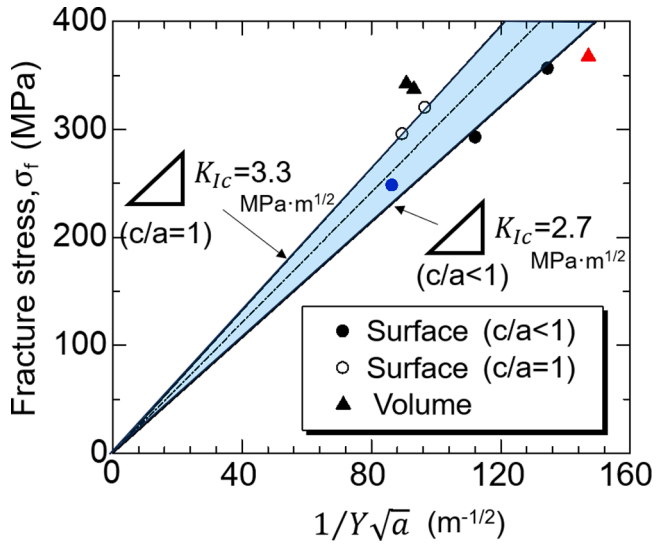

Fig. 18. Relation between fracture stress and $1/Y\sqrt{a}$ by assuming the elliptical crack model.

size. They supposed the crack-tip toughness of alumina (K_0 = 2.3 MPa·m$^{1/2}$ [38]) determines the crack instability for flaws growing around large pores since the contribution of the term $K_\mu(a)$ is relatively small. They suggested that fractures occurred more likely in the semicircular configuration than in the annular crack configuration. The length of a semicircular crack was supposed to scale with the average grain size.

Ozaki [16,43] extended the model to ellipsoidal pores with a major axis radius R (=R_a) and a minor axis radius R_b, as illustrated in Fig. 19 (c). He measured the Weibull distribution of bending strength of almost fully dense alumina with different grain sizes, equivalent to samples sintered at 1400, 1500, and 1600 °C in the present study. The ellipsoidal pore's size and aspect ratio distribution were observed and approximated by appropriate probability density functions. The Weibull strength distribution was predicted from the probability density functions of ellipsoidal pores, fracture toughness of 4.0 MPa·m$^{1/2}$, and the initial crack length corresponding to the grain size. The numerically created Weibull distribution could predict the strength scatter observed experimentally.

Ito, Osada, and Ozaki [44] reported that the fracture from the internal ellipsoidal pore with annular cracks could explain the strength of notched bending specimens as a function of equivalent crack length by assuming fracture toughness of 3.16 MPa·m$^{1/2}$ for alumina. In conclusion, the strength of alumina can be predicted by both the elliptical crack model and the pore-crack model, although the fitting parameter, fracture toughness, differs; it is around 2.7 – 3.3 MPa·m$^{1/2}$ for the former and 3.16 – 4.0 MPa·m$^{1/2}$ for the latter.

5. Concluding remarks

This study utilized synchrotron X-ray multiscale tomography to investigate the evolution of internal structures and defects during the sintering of a high-purity submicron alumina powder. Key findings include the identification of complex pores evolved from transition alumina aggregates and plate-like agglomerates within the initial packing structure, which were observed through micro-CT and nano-CT. These advanced imaging techniques revealed the evolution of defects, including the coarsening of complex pores, which was quantified using mean intercept length and Euler characteristic analysis.

It was shown that complex pores act as potential fracture origins, with circumferential cracks forming at the interface between the pore and matrix. Additionally, defects from plate-like agglomerates were observed to influence fracture behavior. These results provide critical insights into pore evolution, fracture origins, and defect formation, enhancing our understanding of material behavior during sintering.

The integrated approach of high-resolution imaging and fracture

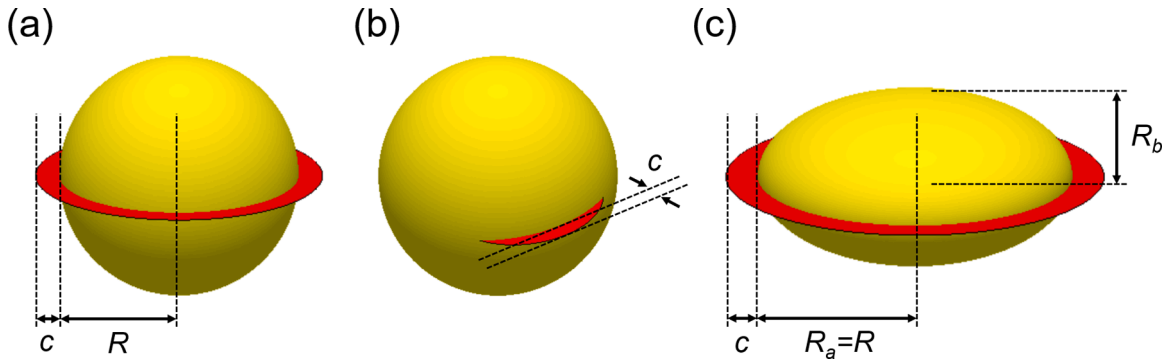

Fig. 19. Pore-crack model. (a) a spherical pore with an equatorial annular crack [38,39], (b) semicircular cracks near a spherical pore [39,40], (c) ellipsoidal pore with an equatorial annular crack [14,42].

analysis presented in this work provides a powerful framework for understanding and controlling defect evolution during sintering. These insights will contribute to the development of more reliable and high-performance ceramics for a broad range of industrial applications.

CRediT authorship contribution statement

Gaku Okuma: Writing – review & editing, Visualization, Supervision, Methodology, Funding acquisition, Data curation, Writing – original draft, Validation, Project administration, Investigation, Formal analysis, Conceptualization. **Tsukasa Shimizugawa**: Writing – original draft, Methodology, Investigation, Formal analysis, Data curation. **Shingo Ozaki**: Writing – review & editing, Methodology, Formal analysis, Data curation. **Toshio Osada**: Writing – review & editing, Investigation, Formal analysis, Data curation. **Shingo Machida**: Visualization, Investigation, Writing – review & editing. **Yutaro Arai**: Investigation, Writing – review & editing, Visualization. **Ryo Inoue**: Writing – review & editing, Visualization, Investigation. **Hideki Kakisawa**: Writing – review & editing, Visualization, Funding acquisition. **Yuki Sada**: Writing – review & editing, Visualization. **Masayuki Uesugi**: Writing – review & editing, Visualization. **Akihisa Takeuchi**: Writing – review & editing, Visualization. **Fumihiro Wakai**: Writing – review & editing, Writing – original draft, Validation, Supervision, Methodology, Formal analysis, Data curation.

Declaration of Competing Interest

The authors declare that they have no known competing financial interests or personal relationships that could have appeared to influence the work reported in this paper

Acknowledgements

The X-ray CT experiments at SPring-8 were performed with the approval of JASRI: Grant Nos. 2022A1115, 2023A1412 and 2023B1214. The authors are deeply grateful to Mr. Takahumi Kawano for obtaining X-ray CT data. We also express our gratitude to Ms. Mariko Iguchi and Mr. Takuma Kohata for their experimental assistance and technical guidance with the SEM observations. This work was supported by JSPS KAKENHI (Grant number JP22K14494). Part of this work is based on results obtained from a project, JPNP22005, commissioned by the New Energy and Industrial Technology Development Organization (NEDO).

Appendix A. Supporting information

Supplementary data associated with this article can be found in the online version at doi:10.1016/j.jeurceramsoc.2025.117679.

References

[1] F.W. Dynys, J.W. Halloran, Compaction of aggregated alumina powder, J. Am. Ceram. Soc. 66 (1983) 655–659.
[2] F.W. Dynys, J.W. Halloran, Influence of aggregates on sintering, J. Am. Ceram. Soc. 67 (1984) 596–601.
[3] A.G. Evans, Structural reliability: a processing-dependent phenomenon, J. Am. Ceram. Soc. 65 (1982) 127–137.
[4] A.G. Evans, Considerations of inhomogeneity effects in sintering, J. Am. Ceram. Soc. 65 (1982) 497–501.
[5] R. Raj, R.K. Bordia, Sintering behavior of bi-modal powder compacts, Acta Met. 32 (1984) 1003–1019.
[6] F.F. Lange, M. Metcalf, Processing related fracture origins: II, agglomerate motion and cracklike internal surfaces caused by differential sintering, J. Am. Ceram. Soc. 66 (1983) 398–406.
[7] G.D. Quinn, Fractograph of Ceramics and Glasses, NIST Special Publication 960-16. National Institute of Standards and Technology, 2007.
[8] G. Okuma, M. Endo, H. Minagawa, R. Inoue, H. Kakisawa, T. Kohata, T. Osada, T. Yamamoto, M. Azuma, A. Takeuchi, M. Uesugi, O. Guillon, F. Wakai, 3D visualization of morphological evolution of large defects during spark plasma sintering of alumina granules, Adv. Eng. Mater. 25 (2023) 2201534.
[9] G. Okuma, T. Osada, H. Minagawa, Y. Arai, R. Inoue, H. Kakisawa, K. Shimoda, A. Takeuchi, M. Uesugi, S. Tanaka, F. Wakai, Heterogeneities and defects in powder compacts and sintered alumina bodies visualized by using the synchrotron X-ray CT, J. Eur. Ceram. Soc. 43 (2023) 486–492.
[10] G. Okuma, R. Usukawa, T. Osada, N. Kondo, H. Nakajima, T. Okazaki, S. Machida, Y. Arai, R. Inoue, H. Kakisawa, K. Shimoda, A. Takeuchi, M. Uesugi, F. Wakai, Evolution of microstructure and defects in sintering of tape-cast alumina laminates observed by synchrotron X-ray multiscale tomography, Ceram. Int. 50 (2024) 37402–37411.
[11] A.M. Venkatesh, R. Barbano, D. Bouvard, P. Lhuissier, J. Villanova, L. Olmos, Exploring the sintering behavior of a complex ceramic powder system using in-situ X-ray nano-tomography, J. Eur. Ceram. Soc. 44 (2024) 7236–7245.
[12] M. Kitayama, J.A. Pask, Formation and control of agglomerates in alumina powder, J. Am. Ceram. Soc. 79 (1996) 2003–2011.
[13] R. Danzer, T. Lube, P. Supancic, R. Damani, Fracture of Ceramics, Adv. Eng. Mater. 10 (2008) 275–298.
[14] S. Fujiwara, Y. Tamura, H. Maki, N. Azuma, Y. Takeuchi, Development of new high-purity alumina, Sumitomo Kagaku 3 (2007) 1–10.
[15] H. Su, D.L. Johnson, Master sintering curve: A practical approach to sintering, J. Am. Ceram. Soc. 79 (1996) 3211–3217.
[16] S. Ozaki, K. Yamagata, C. Ito, T. Kohata, T. Osada, Finite element analysis of fracture behavior in ceramics: Prediction of strength distribution using microstructural features, J. Am. Ceram. Soc. 105 (2022) 2182–2195.
[17] F.F. Lange, Powder processing science and technology for increased reliability, J. Am. Ceram. Soc. 72 (1989) 3–15.
[18] N.M. Alford, J.D. Birchall, K. Kendall, High-strength ceramics through colloidal control to remove defects, Nature 330 (1987) 51–53.
[19] A. Takeuchi, Y. Suzuki, Recent progress in synchrotron radiation 3D–4D nano-imaging based on X-ray full-field microscopy, Microscopy 69 (2020) 259–276.
[20] A. Takeuchi, K. Uesugi, M. Uesugi, H. Toda, K. Hirayama, K. Shimizu, K. Matsuo, T. Nakamura, High-energy X-ray nanotomography introducing an apodization Fresnel zone plate objective lens, Rev. Sci. Instrum. 92 (2021) 023701.
[21] P. Pardo, J. Alarcon, Thermal stability of transition alumina nanocrystals with different microstructures, Ceram. Int. 44 (2018) 11486–11496.
[22] F.W. Dynys, J.W. Halloran, Alpha alumina formation in alum-derived gamma alumina, J. Am. Ceram. Soc. 65 (1982) 442–448.
[23] Y.-C.K. Chen-Wiegart, S. Wang, Y.S. Chu, W. Liu, I. McNulty, P.W. Voorhees, D. C. Dunand, Structural evolution of nanoporous gold during thermal coarsening, Acta Mater. 60 (2012) 4972–4981.
[24] J. Erlebacher, Mechanism of coarsening and bubble formation in high-genus nanoporous metals, Phys. Rev. Lett. 106 (2011) 225504.
[25] F. Wakai, M. Yoshida, Y. Shinoda, T. Akatsu, Coarsening and grain growth in sintering of two particles of different sizes, Acta Mater. 53 (2005) 1361–1371.

[26] G. Okuma, N. Saito, K. Mizuno, Y. Iwazaki, H. Kishi, A. Takeuchi, M. Uesugi, K. Uesugi, F. Wakai, Microstructural evolution of electrodes in sintering of multi-layer ceramic capacitors (MLCC) observed by synchrotron X-ray nano-CT, Acta Mater. 206 (2021) 116605.
[27] G. Okuma, S. Tanaka, F. Wakai, Domain coarsening in viscous sintering as a result of topological pore evolution, J. Eur. Ceram. Soc. 42 (2022) 729–733.
[28] R.T. DeHoff, F.N. Rhines, Quantitative Microscopy, McGraw-Hill Publishing, 1968.
[29] G. Okuma, D. Kadowaki, T. Hondo, S. Tanaka, F. Wakai, Interface topology for distinguishing stages of sintering, Sci. Rep. 7 (2017) 11106.
[30] C. Legros, C. Carry, S. Lartigue-Korinek, P. Bowen, Phase transformation and densification of nanostructured alumina. Effect of seeding and doping, Defect Diffus. Forum 237-240 (2005) 665–670.
[31] ASTM, West Conshohocken, PA, 2002.
[32] J.C. Newman, I.S. Raju, Stress-intensity factor equations for cracks in three-dimensional - finite bodies subjected to tension and bending loads. Computational Methods. pp. 311-334, in the Mechanics of Fracture, Elsevier Science Publishers, BV, 1986.
[33] B. Mussler, M.V. Swain, N. Claussen, Dependence of fracture toughness of alumina on grain size and test technique, J. Am. Ceram. Soc. 65 (1982) 566–572.
[34] W. Yao, J. Liu, T.B. Holland, L. Huang, Y. Xiong, J.M. Schoenung, A.K. Mukherjee, Grain size dependence of fracture toughness for fine grained alumina, Scr. Mater. 65 (2011) 143–146.
[35] A. Muchtar, L.C. Lim, Indentation fracture toughness of high purity submicron alumina, Acta Mater. 46 (1998) 1683–1690.
[36] H. Tomaszewski, M. Boniecki, H. Weglarz, Effect of grain size on R-curve behavior of alumina ceramics, J. Eur. Ceram. Soc. 20 (2000) 2569–2574.
[37] P. Chantikul, S.J. Bennison, B.R. Lawn, Role of grain size in the strength and R-curve properties of alumina, J. Am. Ceram. Soc. 73 (1990) 2419–2427.
[38] J. Seidel, J. Rödel, Measurement of crack tip toughness in alumina as a function of grain size, J. Am. Ceram. Soc. 80 (1997) 433–438.
[39] F.I. Baratta, stress intensity factor estimates for a peripherally cracked spherical void and a hemispherical surface Pit, J. Am. Ceram. Soc. 61 (1978) 490–493.
[40] A.G. Evans, D.R. Biswas, R.M. Fulrath, Some effects of cavities on the fracture of ceramics: II, spherical cavities, J. Am. Ceram. Soc. 62 (1979) 101–106.
[41] A. Zimmermann, M. Hoffman, B.D. Flinn, R.K. Bordia, T. Chuang, E.R. Fuller, Jr, J. Rödel, Fracture of alumina with controlled pores, J. Am. Ceram. Soc. 81 (1998) 2449–2457.
[42] B.D. Flinn, R.K. Bordia, A. Zimmermann, J. Rödel, Evolution of defect size and strength of porous alumina during sintering, J. Eur. Ceram. Soc. 20 (2000) 2561–2568.
[43] S. Ozaki, Y. Aoki, T. Osada, K. Takeo, W. Nakao, Finite element analysis of fracture statistics of ceramics: effects of grain size and pore size distributions, J. Am. Ceram. Soc. 101 (2018) 3191–3204.
[44] C. Ito, T. Osada, S. Ozaki, Finite element analysis of fracture behavior in ceramics: competition between artificial notch and internal defects under three-point bending, Ceram. Int. 48 (2022) 36460–36468.